lubricants

MDPI

Article

Comparative Study on the Leakage Characteristics and Parameter Influence of Bio-Inspired Fishway Staggered Labyrinth Seals

Zhentao Yu [1], Jinbo Jiang [1,*], Xuan Zhang [2], Mengli Zhang [1] and Canlong Li [1]

[1] School of Mechanical Engineering, Zhejiang University of Technology, Hangzhou 310023, China; yuzhentao314@163.com (Z.Y.); 15168302156@163.com (M.Z.); licanlong000@163.com (C.L.)
[2] College of Optical, Mechanical and Electrical Engineering, Zhejiang A & F University, Hangzhou 311300, China; 20220059@zafu.edu.cn
* Correspondence: jiangjinbo@zjut.edu.cn

Abstract: Innovating seal structures and optimizing size parameters are effective ways to enhance the leakage characteristics of labyrinth seals (LSs). Inspired by the ecological fishways with high flow resistance on dam sides, a novel bio-inspired staggered labyrinth seal is proposed. The leakage characteristics of both the curved-edged bio-inspired labyrinth seal (CELS) and the straight-edged bio-inspired labyrinth seal (SELS) at different tooth-incline angles are studied numerically and experimentally. The influence of key geometrical parameters on the leakage characteristics and flow field parameters of the CELSs are investigated, and the leakage control mechanism of bio-inspired LSs is revealed via analyzing flow field parameter distribution. The results indicate that, compared to conventional double-sided staggered straight-tooth labyrinth seals, the leakage rate reduction in CELSs is up to 30% when the incline angle is equal to 25°, outperforming that of the SELS in leakage control. This improvement is mainly attributed to the flow path bending and jet contraction effects at the tooth-tip entrance, along with the thermodynamic effects of the high-turbulence dissipation zone adjacent to the tooth top. The optimum leakage characteristics can be achieved when seal clearance $h < 0.5$ mm, aspect ratio $\delta < 0.6$, and tooth thickness $t < 1.5$ mm. This work provides new insights into the structural design of high-resistance and low-leakage labyrinth seals.

Keywords: staggered labyrinth seals; leakage characteristics; ecological fishway; jet contraction effect

check for updates

Received: 28 December 2024
Revised: 19 January 2025
Accepted: 12 February 2025
Published: 20 February 2025

Citation: Yu, Z.; Jiang, J.; Zhang, X.; Zhang, M.; Li, C. Comparative Study on the Leakage Characteristics and Parameter Influence of Bio-Inspired Fishway Staggered Labyrinth Seals. *Lubricants* **2025**, *13*, 95. https://doi.org/10.3390/lubricants13030095

Copyright: © 2025 by the authors. Licensee MDPI, Basel, Switzerland. This article is an open access article distributed under the terms and conditions of the Creative Commons Attribution (CC BY) license (https://creativecommons.org/licenses/by/4.0/).

1. Introduction

Labyrinth seals (LSs) are widely utilized in the shaft ends, inter-stage areas, blade tips, and secondary flow paths of rotating equipment such as steam turbines, gas turbines, and aero-engines due to their simple structure, ease of installation, and high reliability [1–4]. These seals are primarily employed to restrict gas leakage or suppress reverse leakage flow [5]. Single-sided straight-through LSs and hole-pattern damping seals are the current common forms of annular seals. However, they often suffer from strong permeability effects and excessive gas leakage rates. Many researchers have focused on enhancing seal leakage characteristics by innovating the structural form of labyrinth tooth chambers or damping holes and optimizing geometrical parameters. The influence of tooth incline on leakage characteristics has attracted significant attention. Huo [6] compared the leakage rate and dynamic characteristics of three labyrinth seal types, including isosceles trapezoid teeth (ITST), front right-angled trapezoid teeth (FRTST), and rear right-angled trapezoid teeth (RRTST), finding that FRTST demonstrated the lowest leakage rate due to their larger

divergence angle and stronger energy dissipation. Zhang [7] studied the influence of geometrical parameters on the leakage characteristics of inclined-tooth LSs experimentally, identified sensitivity rankings, and obtained optimal values for key structural parameters. Chougule [8] optimized the shape of inclined tooth tips to enhance vorticity dissipation, achieving a reduction of 9% in leakage rate. Zhang [9] explored the effects of axial incline in damping holes on leakage characteristics, highlighting that inclined holes enhance cavity vorticity dissipation compared to straight holes and thereby improve leakage performance. Zhao [10] conducted a comprehensive and in-depth optimization study on six key design variables for straight-tooth labyrinth seals, and this optimization approach successfully reduced the leakage coefficient and clarified the influence patterns of various variables. Kim [11] investigated the effects of geometric factors on the mass flow in honeycomb-toothed labyrinth seals, finding that the mass flow of honeycomb-toothed labyrinth seals reaches its minimum at a tooth fore angle of 60°.

Traditionally, labyrinth seals are equipped with single-sided tooth chambers or damping hole structures. However, the introduction of dissipative tooth or hole structures on both the stator and rotor surfaces, through designs such as labyrinth-honeycomb seals or double-sided labyrinth seals, has roused considerable attention. Zhang [12] found that double-sided hole-damping seals outperform single-sided hole-damping seals in leakage control capacity when the seal clearance is relatively large. Gu [13] proposed a fluidic oscillation seal concept, which significantly dampens kinetic energy increase by innovatively designing dual-side labyrinth tooth chambers and recirculation channels. It has been recognized that employing double-staggered teeth to suppress straight-through leakage flows can substantially reduce leakage. Comparative studies of rotor single-tooth, stator single-tooth, and double-staggered tooth LSs have shown that double-staggered configurations possess the significantly lowest leakage rate, followed by the stator tooth one [14,15]. A conjugated heat transfer model was employed by Liu [16,17] to analyze the leakage flow and heat transfer characteristics of staggered honeycomb labyrinth seals, highlighting that the turbulent dissipation induced by fluctuations plays a principal role in energy dissipation. Optimizing the tooth structures and chamber shapes of double-staggered LSs to further strengthen the leakage control capacity is an area of interest. Jia [18] replaced rotor straight teeth with T-shaped teeth, achieving a 25% reduction in the leakage rate compared to straight-through seals, yet still larger than double-staggered straight teeth. Yan [19] substituted straight teeth on both seal surfaces with semi-elliptical teeth and pointed out that this novel design exhibited higher stability under positive axial displacement than that of the conventional design while lacking a comparative study on leakage characteristics. Retaining straight teeth on the stator surface and replacing rotor straight teeth with semi-Y-shaped or bow-shaped auxiliary inclined teeth resulted in over 40% leakage reduction compared to straight-through seals [20,21]. This demonstrated the significant potential for enhancing leakage characteristics through modifications in staggered LS tooth designs. Moscatelli [22] employed intelligent algorithms to conduct topology optimization on flow paths of staggered LSs, revealing that the optimal leakage rate was achieved with complex curved edges rather than straight edges. However, the clear design methodology for tooth chamber shapes in LS has not been proposed.

Inspired by biological structures with exceptional functional characteristics in nature, the bionic seal structure and flow path design have displayed considerable advantages in structural strengthening and enhancing film stability. Cao [23] developed a bionic layered LS structure, simulating a snail shell with load-bearing outer surfaces and an insulating inner core, achieving combined sealing strength and thermal insulation. Jiang [24,25] designed several surface groove face structures for dry gas seals inspired by bird wing shape, developing a bionic wing-shaped groove dry gas seal that demonstrated a 20%

larger film stiffness than a typical spiral groove dry gas seal. Ecological fishways designed to facilitate fish migration across dams are typical high flow-resistance structures that achieve reduced water flow speed, allowing weak swimming species to ascend streams [26]. This is similar in principle to Tesla valve flow structures [27,28], which strengthen flow resistance through impact losses and vortex dissipation in curved paths, finding successful application in cooling plates [29], pulsating heat pipes [30], and check valves [31]. Wang [32,33] developed a series of high-resistance, self-impacting clearance seal structures based on Tesla valve principles, using primary and secondary flow self-impacts to enhance energy dissipation, yielding substantial leakage reduction. However, the complexity and installation difficulty of these structures somewhat limit their application in turbomachinery. Exploring how ecological fishways with high flow resistance properties can be applied to staggered LS flow path design to develop simple, high-resistance, and effective leakage control seals is still a subject for further investigation.

This study draws inspiration from high-resistance ecological fishways and designs a novel fishway-inspired staggered labyrinth seal structure innovatively. A comparative analysis of the leakage characteristics of both curved-edge and straight-edge fishway labyrinth seals under different tooth incline angles is numerically studied utilizing commercial software. The leakage control mechanism of LSs with various structures is revealed by analyzing the velocity field distribution, turbulence dissipation rate, and viscosity distribution within the seal tooth chambers and clearance. This study further explores the impact of key geometrical parameters, including seal clearance, the tooth chamber aspect ratio, the inlet coefficient, and tooth thickness, on the leakage characteristics and flow field distribution of CELSs, and validates the numerical results by measuring the leakage rate at different tooth incline angles of CELSs.

2. Numerical Simulation Model of Labyrinth Seal

2.1. Structural Model

In nature, high-built dams obstruct the migratory path of fish, while the ecological fishways on both sides of the dam provide migratory fish with a pathway to swim upstream. Water from high levels flows downward along the fishway due to gravity. However, the high flow velocity poses significant resistance to fish swimming upstream. Hence, increasing the resistance to water flow in the fishway to achieve lower velocities is crucial. Figure 1 illustrates a typical high-resistance labyrinthine ecological fishway, composed of multiple serially arranged flow channel units with height differentials and crescent-shaped cross-sections. Adjacent crescent-shaped channels are staggered to form a labyrinthine passageway, interconnected by narrower slit-like channels. This design enhances flow resistance by generating vortices within the crescent-shaped channels, while the narrower connecting passages narrow the flow channel, consequently lowering the flow velocity.

Labyrinth seals, widely used in rotating turbomachinery, share structural and functional similarities with ecological fishways. While ecological fishways reduce water flow velocity driven by gravity through shape design, labyrinth seals reduce the gas flow velocity and flow rate under pressure differentials through the seal structure design. The common objective for both systems is to increase flow resistance to diminish the flow velocity and rate. Inspired by the high-resistance features of ecological fishways, a novel fishway-inspired staggered labyrinth seal (FSLS) structure has been developed, as shown in Figure 2. A typical FSLS comprises a sealing pair formed by a rotor and a stator, equipped with curved labyrinth teeth. These teeth are staggered axially on the seal surfaces. The windward side of the curved teeth and the leeward side of the mating curved teeth create a curved-edge sealing chamber, allowing gas to form vortices within the tooth cavity and dissipate energy, akin to the crescent-shaped units in ecological fishways. Furthermore,

the apex of the curved teeth and the surface of the mating sealing pair maintain a narrow sealing gap, which induces local flow resistance and narrows the flow channel, resembling the slit-like channels connecting adjacent fishway units.

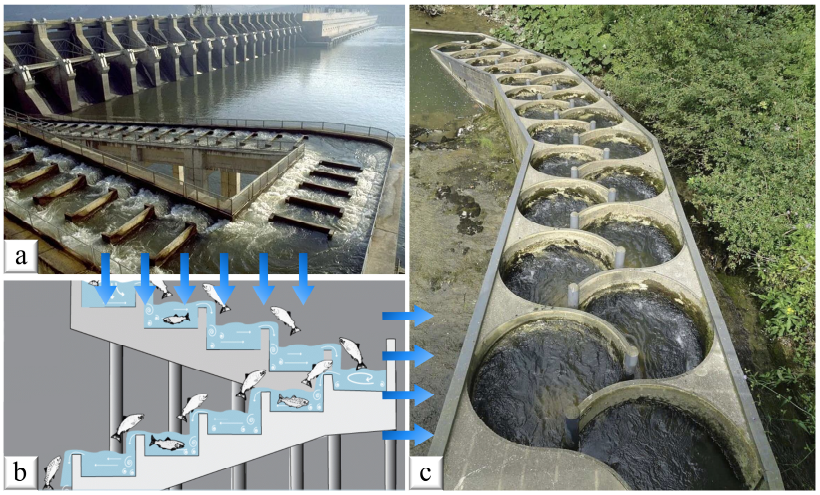


Figure 1. A dam in nature and its labyrinthine ecological fishway used for fish migration. (**a**) The dam and the fishway. (**b**) the working principle of the ecological fishway (**c**) the crescent-shaped staggered fishway with high flow resistance.

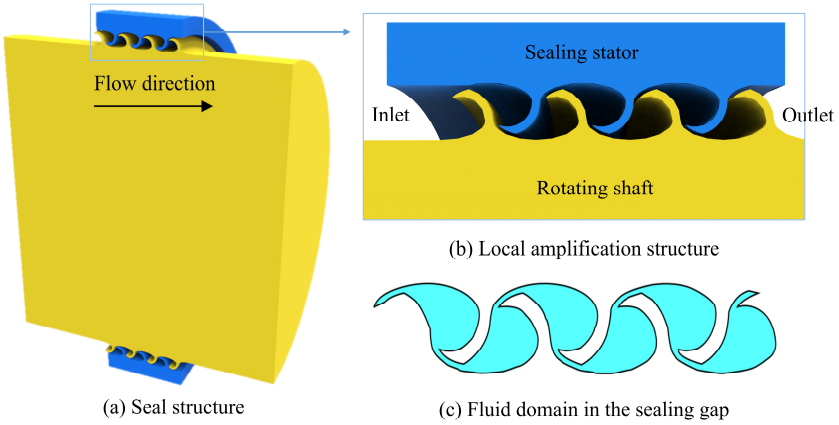
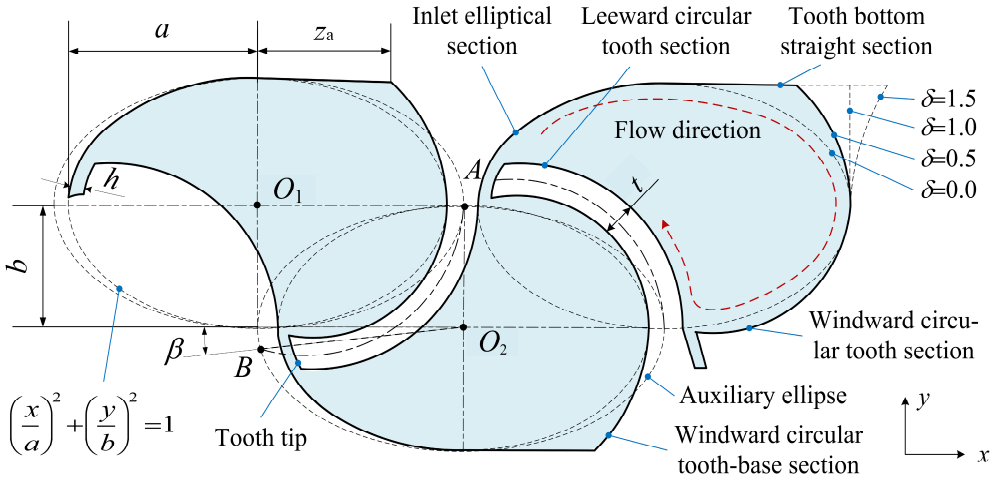


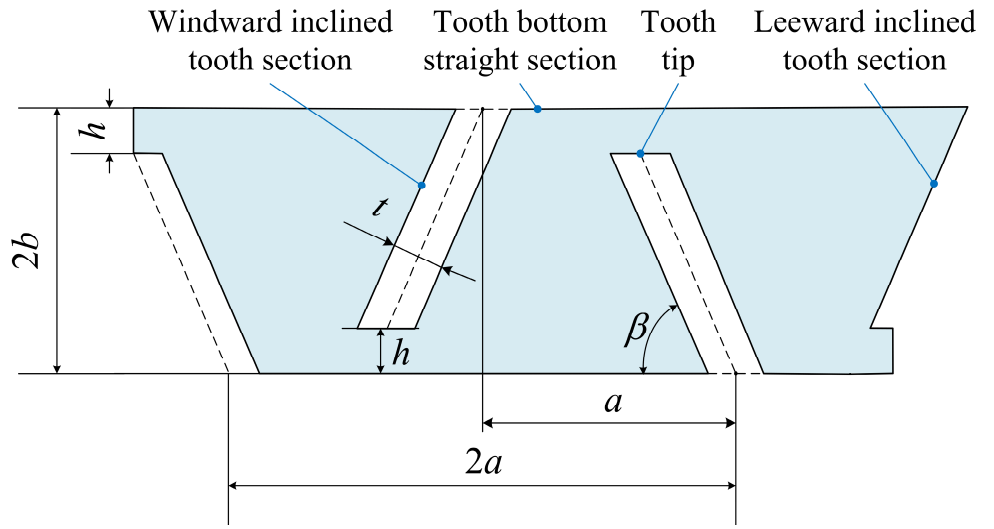
Figure 2. 3D structural model of the staggered labyrinth seal inspired by fishways.

Figure 3 presents two typical geometrical models of fluid domains for fishway-inspired staggered labyrinth seals: the CELS and the SELS. For the seal cavity of the CELS, the sequence along the leakage flow direction includes an inlet elliptical section, a tooth-bottom straight section, a windward circular tooth-base section, a windward circular tooth section, and a leeward circular tooth section. The basic shape of the labyrinth tooth cavity is an ellipse with semi-major and semi-minor axes of lengths a and b, respectively. The centers of adjacent tooth cavity ellipses are denoted as O_1 and O_2. The aspect ratio w of the tooth cavity is defined as the ratio of semi-minor axis b to semi-major axis a. The curved-edge labyrinth tooth thickness is t, with a seal clearance h between the tooth tip and the mating surface. The surfaces on either side of the labyrinth tooth are the windward curved tooth surface and the leeward curved tooth surface. A virtual ellipse, concentric with the inlet ellipse and tangent at point A to the midline of the tooth thickness, has a semi-major axis of $(a + t/2)$ and a semi-minor axis of b. The midline of the curved tooth thickness intersects the virtual ellipse at point B. The incline angle β is defined between line BO_2 and the opposite direction of the elliptical major axis x. When $\beta = 90°$, the labyrinth tooth is straight. To enhance the geometric representational ability of the seal structure, a tooth base straight

segment with length z_a is added between the elliptical inlet section and the windward tooth root segment. The inlet coefficient δ is the ratio of the tooth base straight segment length z_a to the ellipse's semi-major axis length a. When $\delta = 0$ and $\delta = 1$, the windward tooth root segment is elliptical and straight, respectively.



(**a**) Curved-edge tooth labyrinth seal.



(**b**) Straight-edge tooth labyrinth seal

Figure 3. Structural model of fishway-inspired labyrinth seals along with parameter definitions.

For the seal cavity of the SELS, the tooth cavity is trapezoidal, enclosed by a windward inclined tooth section, a leeward inclined tooth section, a rotor tooth base surface, and a stator tooth base surface. The distance in the x direction between adjacent seal teeth on the same seal surface and adjacent seal surfaces is $2a$ and a, respectively. Moreover, the distance in the y direction between the tooth base surfaces of the two seal surfaces is $2b$. The seal tooth thickness and the tooth-tip clearance are t and h, respectively. The angle between the seal tooth and the opposite direction of the x-axis is β. When $\beta = 90°$, the configuration is a staggered straight-tooth labyrinth seal, the commonly used seal form in inter-stage and shaft-end seals of turbines.

Table 1 presents the initial geometric parameters and operating conditions used in the numerical simulations in this study. Unless specified otherwise, the parameters listed in the table are used as default values.

Table 1. Geometrical parameters and working conditions.

Parameters and Symbols	Values	Parameters and Symbols	Values
Inlet pressure p_{in}/MPa	0.3	Tooth thickness t/mm	1
Outlet pressure p_{out}/MPa	0.15	Aspect ratio w	0.4
Inlet temperature T/K	293	Inlet factor δ	0
Seal clearance h/mm	0.5	Fluid domain width d/mm	10
Inclined angle β/°	5	Semi-major axis length $2a$/mm	10

The selection of the working medium is of paramount importance in the context of the study. In this case, ideal air has been chosen as the working medium. The physical parameters of this ideal air are detailed in Table 2. These parameters collectively govern the fluid's behavior, including its flow characteristics, heat transfer capabilities, and viscous effects. The choice of ideal air as the working medium, with its well-defined and measurable physical properties, allows for more accurate and reliable analysis and simulation of the system under consideration, facilitating a better understanding of the underlying physical phenomena and enabling the optimization of the system's performance.

Table 2. Physical parameters of ideal air.

Parameters and Symbols	Values	Parameters and Symbols	Values
Temperature t/°C	25	Thermal diffusivity $D_T/10^{-2}$ m^{2}h^{-1}	7.900
Density ρ/kg·m^{-3}	1.146	Dynamic viscosity $\mu/10^{-6}$ Pa·s	18.486
Thermal conductivity C_p/kJ·(kg·K)$^{-1}$	1.013	Kinematic viscosity $v/10^{-6}$ m^{2}s^{-1}	16.155

To address the challenge of disassembling and assembling double-sided staggered tooth labyrinth seals, which previously could only employ an upper and lower split stator design and were difficult to install from one side, a novel axial modular labyrinth tooth structure is proposed, as depicted in Figure 4. A space is created between the shaft sleeve and the sealing chamber to accommodate the installation of the sealing tooth components. These components, consisting of single-tooth rotor and stator elements, are sequentially stacked in an axial arrangement. They are secured along the axis by compressing the shaft sleeve and cover plate, aligning multiple rotor and stator teeth in place. Additionally, eccentric plates, which determine the axial relative positions of the rotor and stator, are mounted on the cover plate and can be removed prior to use.

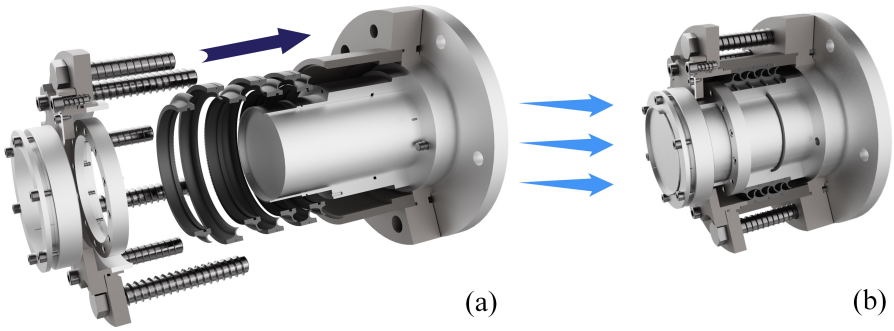


Figure 4. Package type double-sided staggered labyrinth sealing assembly diagram. (**a**) Explosive diagram of the novel axial modular laby-rinth tooth structure. (**b**) Structural section view of the novel axial modular laby-rinth tooth structure.

2.2. Mesh Generation and Boundary Conditions

In this study, the meshing tool of the ANSYS Workbench module was utilized to divide the fluid domain mesh of the FSLS, which consists of six tooth chambers. Considering the uniform structure of the seal along the circumferential direction, a computational domain with a circumferential width of 10 mm was selected to enhance computational efficiency. The influence of circumferential curvature was neglected by designing the sample as a straight plate along the circumferential direction. Figure 5 presents the mesh division results for the fluid domain of the CELS. A structured mesh was used for the overall fluid domain, with local mesh refinement applied to areas with structural discontinuities, such as the sealing gap and their inlet and outlet, to better capture the variations in flow field parameters within these localized regions.

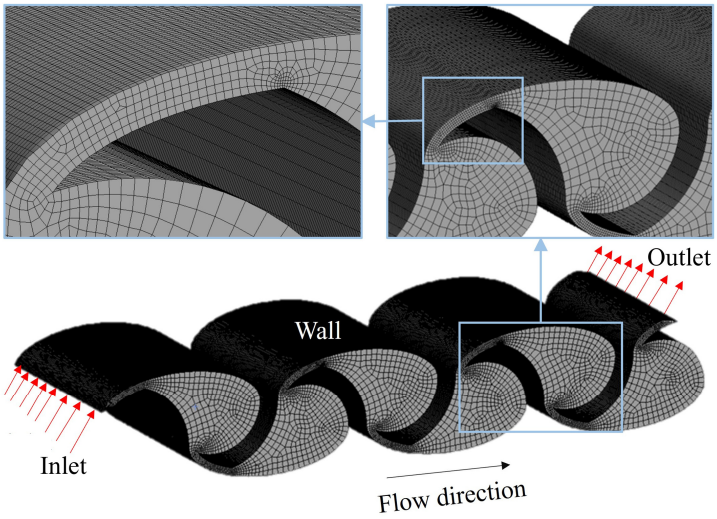


Figure 5. Schematic diagram of mesh division in the fluid domain of the CELS.

The sealing fluid is considered an ideal gas. Boundary conditions were set as the pressure inlet and pressure outlet, with the circumferential sides of the computational domain configured with periodic boundary conditions. The upper and lower seal surfaces were defined as adiabatic solid walls with no-slip conditions. The commercial software Fluent 2022 R1 was employed to simulate the distribution of flow field parameters in the labyrinth seal and calculate the mass leakage rate. Since the flow within the small sealing gap pertains to near-wall flow with significant radial flow parameter variations, improved wall functions were used to replace the standard wall functions. The SST k-ω two-equation turbulence model was chosen for the flow control equation, and the finite volume method was utilized to discretize the control equations. The SIMPLE method was used to solve the pressure and velocity distribution within the sealing fluid domain. The computation was considered converged when the residuals of the continuity, momentum, and turbulence equations were all below the order of 10^{-5}, and the relative mass flow rate error at the inlet and outlet was less than 0.1%.

3. Seal Test for Measuring Leakage Rate

The leakage characteristics of a double-sided staggered labyrinth seal inspired by fishway grooves were simulated under varying rotational speeds, as shown in Table 3, with the speed range spanning from 0 to 6000 rpm. As the rotational speed increases, the leakage rate of the clearance seal shows a slight increase. Compared to the zero rotational speed, the increase in leakage rate does not generally exceed 2%. It is evident that the data obtained at zero speed remain applicable under varying rotational speeds.

Table 3. Variation of leakage rate with different rotating speeds.

Rotating Speed n/(r·min^{-1})	Mass Leakage Rate q_m/(g·s^{-1})
0	17.452
1000	17.558
2000	17.639
3000	17.696
4000	17.760
5000	17.805
6000	17.836

3.1. Experimental Testing System

The accuracy and reliability of the numerical simulation results of the leakage rate of labyrinth seals need to be validated through experimental tests. To facilitate precise control of the seal clearance and reduce testing costs, flat plate samples were used in place of cylindrical seal samples. Figure 6 shows the test system for leakage characteristics of the staggered labyrinth seal with flat plates, comprising three main components: the air supply and exhaust system, the testing system, and the measured seal module. The air supply and exhaust systems provide a controllable and measurable air source for both the inlet pressure and outlet pressure of the measured seal. Compressed air, pressurized by a screw air compressor (11), is dehydrated and filtered before entering an air reservoir (12). It then passes through a pressure regulator (13), a gas flow meter (14), and a digital pressure gauge (15) before entering the measured seals via pneumatic joints. The gas from the left and right pneumatic joints is vented to the atmosphere following passage through a digital pressure gauge, a gas flow meter, and a pressure regulator. The testing system utilizes a data acquisition card (16) to collect voltage outputs from three gas flow meters (14) on the intake and exhaust pipelines and from three miniature pressure sensors (35, 36, and 37) mounted on the lower sample holder. These measurements provide the gas flow rate, inlet pressure, and outlet pressure, transmitting the data to a computer (17) for processing and display. The gas flow meters are MEMS-type mass flow meters with a range of 300 L·min^{-1} and an accuracy of 0.1 L·min^{-1}.

The measured seal module primarily consists of upper and lower seal sample assemblies, surrounded by a seal ring (26) to prevent leakage into the surrounding environment. The upper seal sample assembly includes an upper sample holder (28) and an inset upper seal sample, fixed below the pneumatic joint mount (27) and clamped by four set screws (21) mounted on the screw mount (23), itself affixed to the upper panel (24). The lower seal sample assembly comprises a lower sample holder (31) and an inset lower seal sample, secured to the lower panel (32). The seal ring (26) is installed within a seal mount (25) and clamped by four set screws (22) fastened to the upper panel (24), ensuring a reliable seal around the sealing gap periphery. Pressure measurement holes are positioned on the lower sample holder at the middle inlet and both end outlets, allowing direct and precise pressure measurements on the sealing gap using miniature pressure sensors. This setup avoids inaccuracies in measuring the seal's inlet and outlet pressure indirectly via pipeline pressure gauges, which might be affected by pressure drops due to flow resistance between the pipelines and the seal gap. Two different labyrinth seal structures, designated as (33) and (34), are mounted on the left and right sides, respectively. The seal clearance can be adjusted using spacers installed between the upper and lower seal sample assemblies.

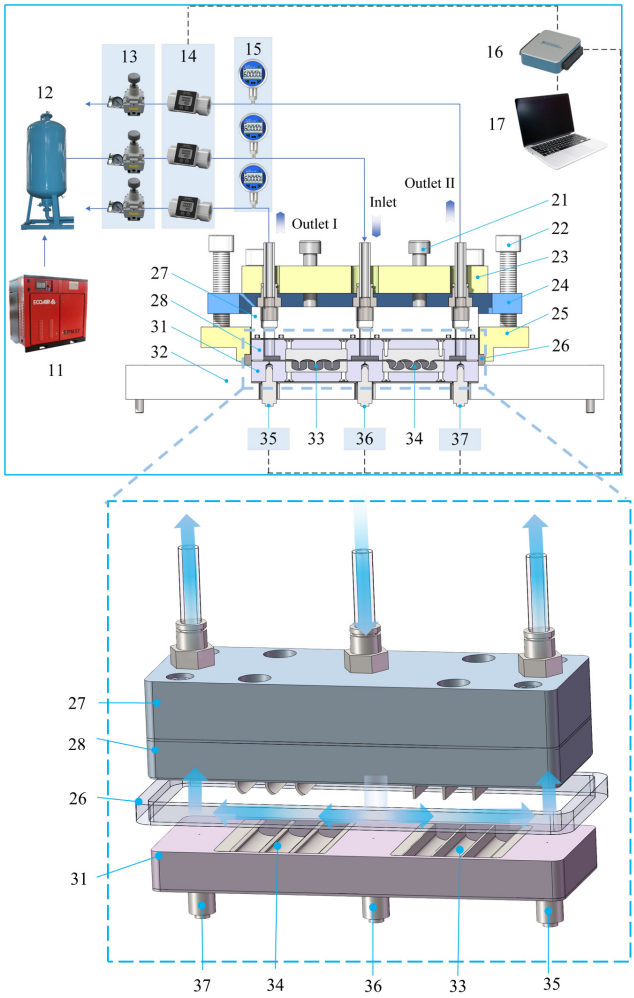


Figure 6. Flowchart of the test system for measuring leakage rate of clearance seals. 11—Air compressor, 12—Air tank, 13—Pressure regulator, 14—Flow meter, 15—Digital pressure gauge, 16—Data acquisition card, 17—Computer, 21—Seal sample tightening screw, 22—O-ring tightening screw, 23—Screw mounting base, 24—Upper panel, 25—O-ring mounting base, 26—O-ring, 27—Pneumatic joint mounting base, 28—Upper sample mounting base, 31—Lower sample mounting base, 32—Lower panel, 33—Left sample assembly, 34—Right sample assembly, 35—Left sample outlet micro-pressure sensor, 36—Middle inlet micro-pressure sensor, 37—Right sample outlet micro-pressure sensor.

3.2. Seal Samples

Due to the complexity of the tooth cavity profiles in the FSLS samples, precision milling with multi-axis machine tools was used to machine concave cavities (concave samples) or protruding teeth (convex samples) from aluminum alloy blanks. These samples were then secured with screws into the rectangular mounting slots of the specimen holders, forming the composite seal samples illustrated in Figure 7. In the upper seal sample assembly with the convex sample, rectangular equalizing grooves were machined near the inlet and outlet air holes of the sample holder to ensure a more uniform pressure distribution at the sealing gap entrance and exit. It is required that the plane of the convex seal teeth root be flush with the seal surface of the sample holder, with a height discrepancy not exceeding 10 μm, to ensure accurate control of the seal clearance. For the lower seal sample assembly with the concave sample, pressure measurement holes with a diameter of 0.5 mm were machined at locations corresponding to the central inlet and side outlets, with installation holes below for mounting miniature pressure sensors. The upper surface of the concave seal sample

is also required to be flush with the sealing surface of the sample holder, with a height discrepancy not larger than 10 μm.

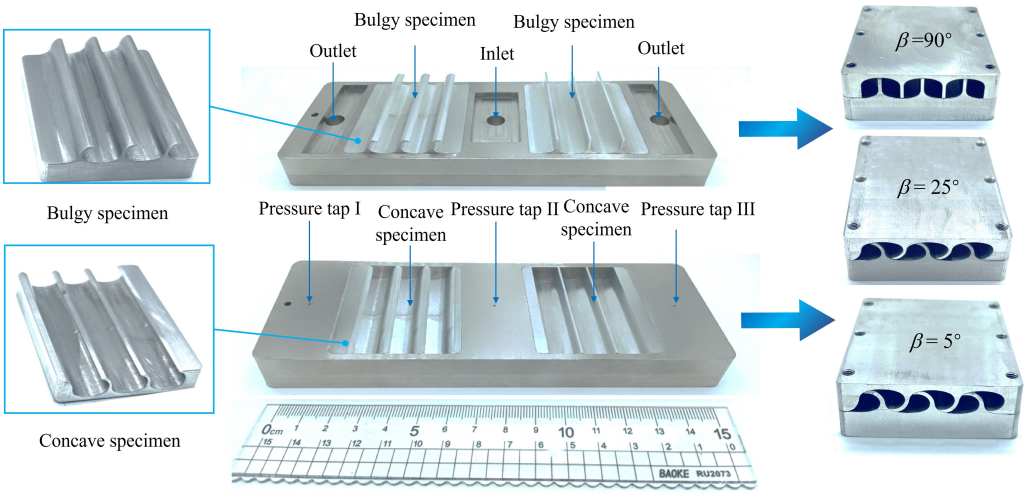


Figure 7. Fishway-inspired staggered embedded composite flat seal sample.

Three sets of seal samples with tooth incline angles of 5°, 25°, and 90° were prepared. When these seal samples are installed in reverse (i.e., swapping the inlet and outlet), samples with incline angles of 175°, 155°, and 90° can be configured, respectively. To avoid mutual interference due to uneven gas flow distribution when testing the two samples simultaneously, only one side's seal leakage rate was tested at a time, with the exhaust port of the other seal sample blocked.

The machining precision of the tooth cavity and labyrinth teeth significantly influences the actual seal clearance during the testing process, with typical machining precision at the 0.01 mm level while the seal clearance is at the 0.1 mm level. Hence, strict control of machining errors is necessary. Considering the high sensitivity of the seal leakage rate to the seal clearance, high-precision measurements were conducted on the machined fishway-inspired seal samples to determine their actual dimensions. Figure 8 shows the two-dimensional projections and three-dimensional scanning tests of the surface profiles of the fishway-inspired seal flat samples. A blue light scanner was used to scan the three-dimensional surface profiles of the concave and convex samples. This method captures the three-dimensional coordinates of surface points unobscured by tooth geometry when horizontally oriented but cannot capture coordinates of obscured regions. Three characteristic planes perpendicular to the leakage direction were selected to obtain height coordinates at different profile points of the concave and convex samples, thereby determining the actual seal clearance at various tooth tops. A digital projector was used to test the projection profiles of samples with differing structures, enabling the quantitative acquisition of coordinate points along the projection contour, although it cannot capture vertical dimensional differences.

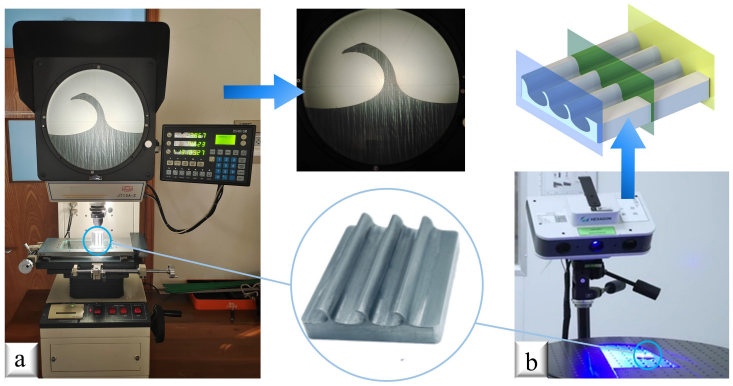
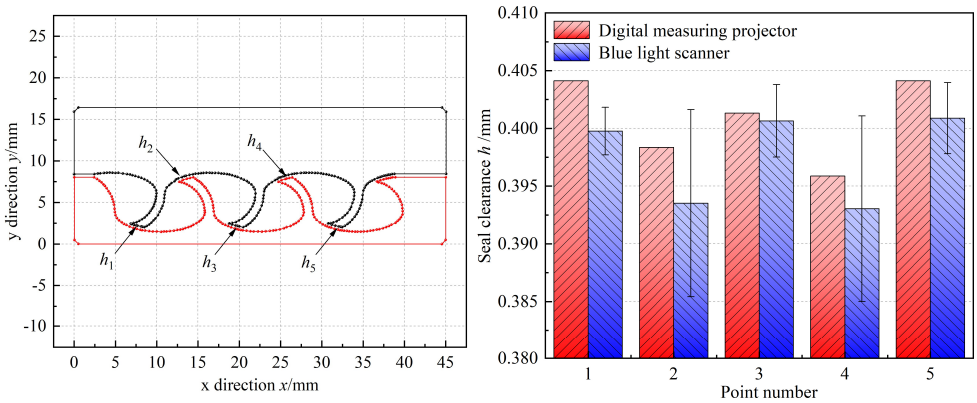


Figure 8. Ultra-precision testing of the surface profile of the flat seal sample. (**a**) The two-dimensional projections of the surface profiles of the fishway-inspired seal flat samples. (**b**) The three-dimensional scanning tests of the surface profiles of the fishway-inspired seal flat samples.

Figure 9 illustrates the surface profiles of the seal samples and different tooth top seal clearance obtained from the above-mentioned method. The seal clearance between the upper and lower samples was adjusted to 0.4 mm using gap adjustment shims. As can be seen, the seal clearance measurements for the tooth tops obtained from the two testing methods align well, with measurement deviations at identical tooth tops not exceeding 5 μm. Examining the distribution of the five-tooth top seal clearance reveals values ranging from 0.393 mm to 0.404 mm, indicating a maximum deviation of approximately 0.01 mm. The relative deviation from a 0.4 mm seal clearance is less than 3%, meeting the experimental requirements.



(**a**) Seal sample profile (**b**) Seal clearance

Figure 9. Surface profile and seal clearance test results of the flat samples based on the two testing methods.

Figure 10 shows the sample assembly of the flat-plate clearance seal and the reliability guarantee method of seal clearance regulation. As can be seen from Figure 10a, the test seal includes, from top to bottom, the pneumatic joint installation seat, upper rubber mat, upper seal sample, gap adjustment gasket, lower seal sample, lower rubber mat, and lower sample seat. The following measures can be taken: (1) using a pointer vernier caliper with a resolution of 0.02 mm, the thickness of the gap adjustment gasket can be tested, and the thickness error is required to be no more than 0.02 mm; (2) after the rough surface sample is installed in the groove on the mounting seat, the height difference between the end face of the sample and the end face of the mounting seat is measured by a dial gauge with a resolution of 1 μm, and the height difference is required to be no more than 0.01 mm. This strict control measure helps to minimize the impact of installation errors on

the actual seal clearance, thereby strengthening the reliability and persuasiveness of our experimental results.

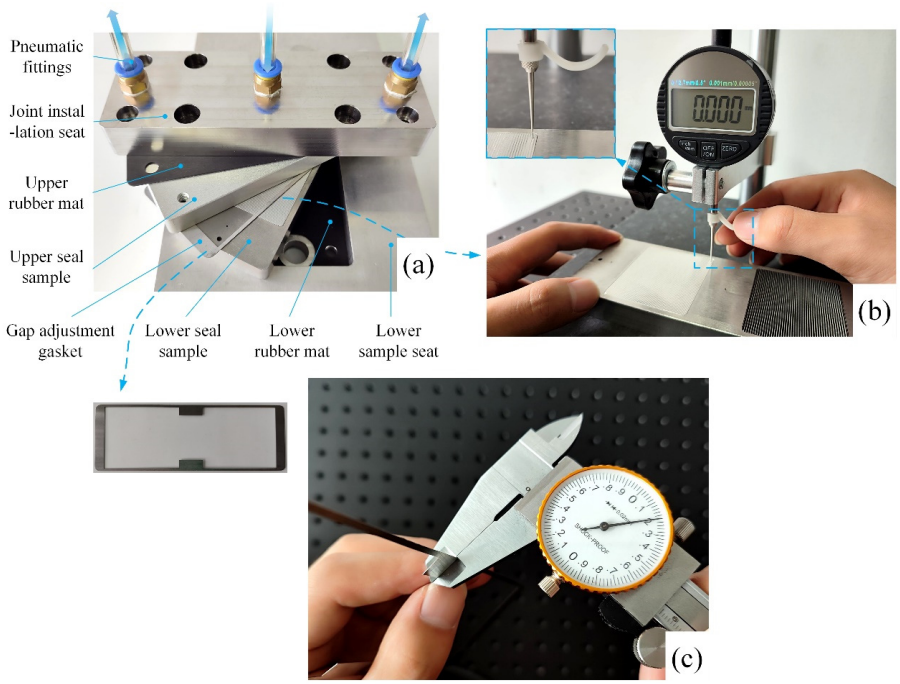


Figure 10. Seal clearance reliability guarantee method for flat plate clearance seal test. (**a**) the sample assembly of the flat-plate clearance seal. (**b**) Measure the height difference between the sample end face and the mounting seat end face using a dial gauge. (**c**) Use vernier calipers to test the thickness of the gap adjustment gasket.

4. Results Analysis and Discussion

A comparative study was conducted to numerically and experimentally investigate the leakage characteristics of the FSLS with varying tooth incline angles. The study explored the effects of primary structural parameters on the leakage properties and flow field distributions of these seals under different seal clearances, as well as the underlying mechanisms.

4.1. Grid Independence Verification

The number of mesh elements in the computational domain significantly impacts the simulation accuracy and computation time of the labyrinth seal leakage characteristics. Using the leakage rate corresponding to a maximum mesh count of 5.74 million as a benchmark, the relative error of the leakage rate for the default geometry of the FSLS with different mesh counts was obtained, as shown in Figure 11. The relative error of the leakage rate exhibits a decelerating decrease with an increasing number of mesh elements. At a mesh count of 2.63 million, the relative error of leakage rate is 0.98% and remains below 1% when the mesh count is larger than 2.63 million. Hence, this mesh count and its corresponding mesh size can be selected for subsequent calculation. It is noteworthy that when geometrical parameter variations result in significant changes to the fluid domain of the seal, maintaining the mesh size of the fluid domain at nearly constant can help preserve computational accuracy.

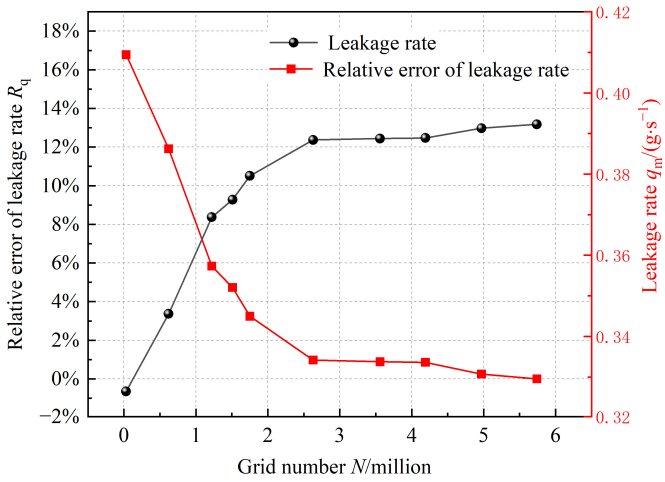
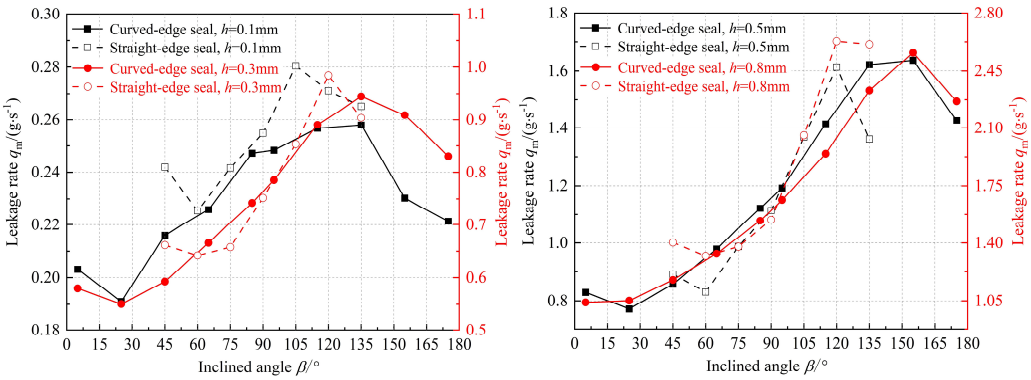


Figure 11. Variation of the relative error of leakage rate with the increasing grid number.

4.2. Performance Comparison Between Straight-Edge and Curved-Edge Seals

The tooth incline angle is a critical factor influencing the leakage characteristics of the FSLS. A comparative study was conducted on the leakage characteristics of the CELS and SELS under various seal clearances and tooth incline angles. Figure 12 illustrates the variation in leakage characteristics of the CELS and SELS with incline angles under seal clearance ranging from 0.1 mm to 0.8 mm. These incline angles for the CELS and SELS range from 5° to 175° and 45° to 135°, respectively.



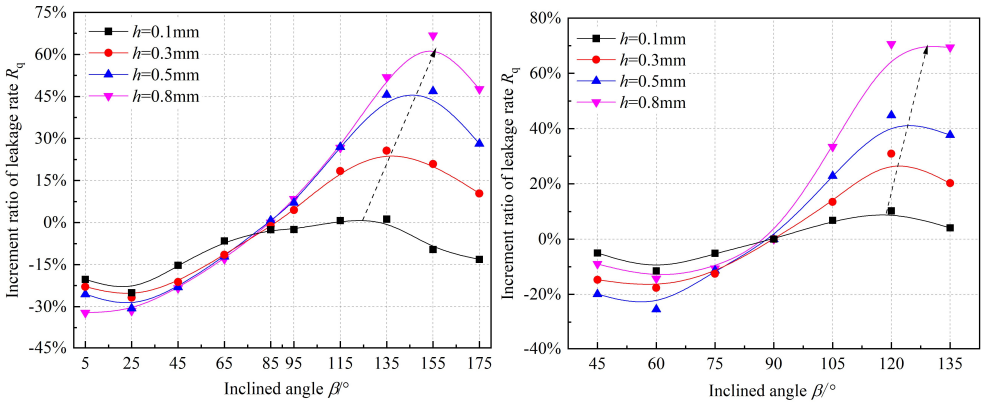
(**a**) Relative small seal clearance (**b**) Relative large seal clearance

Figure 12. Variation of leakage rate with incline angle for CELS and SELS under different seal clearances.

As depicted in the figure, the leakage rates of the two seals exhibit an approximate sinusoidal pattern that first decreases, then increases, and decreases again as the incline angle increases under different seal clearances. The SELS achieves the minimum and maximum leakage rates at incline angles of β = 60° and 120°, respectively. In contrast, the CELS achieves its minimum leakage rate at β = 25° and maximum values at β = 135° to 155°. The minimum leakage rate for the CELS is consistently lower than that of the SELS. However, when β = 90°, there is no significant difference in leakage rates between the two seals. Hence, compared to the SELS, the CELS demonstrates superior capability in flow resistance and leak control.

Considering that a straight-edge, double-sided staggered labyrinth seal with an incline angle of 90° is the most commonly used configuration for shaft end and interstage seals in turbomachinery, the leakage rate of this seal structure under various seal clearances was used as a benchmark in the comparative study. The increment ratio of the leakage rate

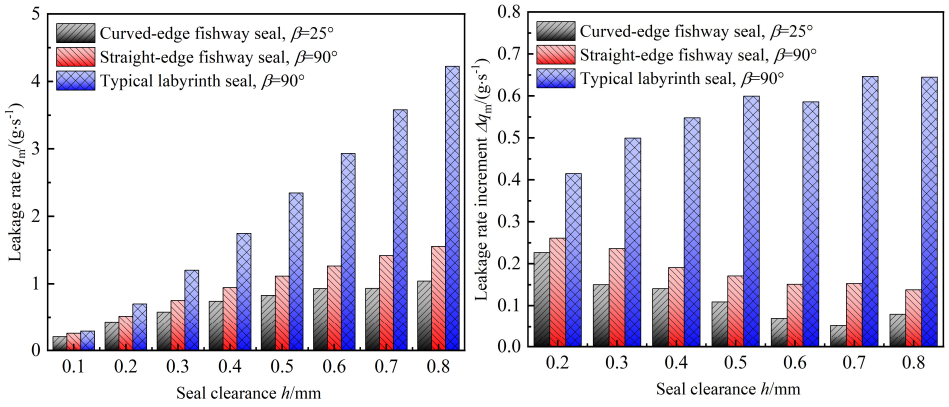
of the FSLS under different seal clearances and incline angles was obtained, as shown in Figure 13. For the SELS, the maximum reduction in leakage rate occurs at $\beta = 60°$, ranging from 10% to 25%. In contrast, the CELS achieves a significantly larger maximum reduction of 25% to 30% at $\beta = 25°$. As the seal clearance increases, the maximum reduction in leakage rate for the two FSLSs shows a slight monotonic increase, while the maximum increase exhibits a significant monotonic rise. For instance, when the seal clearance h increases from 0.1 mm to 0.8 mm, the maximum reduction in leakage rate for the CELS increases from 23% to 31% and the maximum increase rises from 0% to 65%. Furthermore, the optimal incline angles for the minimum leakage rate of the two FSLSs are relatively insensitive to the changes in the seal clearance. However, the incline angle for the maximum leakage rate, termed the worst incline angle, exhibits a monotonic increase with the seal clearance. For example, the worst incline angle for the CELS rises from 125° at $h = 0.1$ mm to 155° at $h = 0.8$ mm.



(**a**) CELS (**b**) SELS

Figure 13. Variation in increment ratios of leakage rate with the incline angle for two typical labyrinth seals.

From the above analysis, it is evident that the relative advantages of the leakage characteristics of different labyrinth seal structures are closely associated with seal clearance. A comparative study was performed on three configurations: a curved-edge, inclined-tooth, fishway-inspired seal at $\beta = 25°$; a curved-edge, straight-tooth, fishway-inspired seal at $\beta = 90°$; and a single-sided, straight-through labyrinth seal at $\beta = 90°$. The leakage rate and its increment variations with increasing seal clearances are illustrated in Figure 14, where the leakage rate increment is defined as the increase in the leakage rate for every 0.1 mm increase in seal clearance. As the seal clearance ranges from 0.1 mm to 0.8 mm, the leakage rate for the typical single-sided seal shows an accelerated increase, while the leakage rate for fishway-inspired labyrinth seals displays a decelerated increase. The leakage rate increment for the straight-tooth FSLS is slightly greater than that of the inclined-tooth FSLS. Furthermore, compared to the inclined-tooth FSLS, when $h = 0.1$ mm, the leakage rate increments for the straight-tooth FSLS and the single-sided labyrinth seal are 25.4% and 41.6%, respectively, and rise to 50.8% and 309.6%, respectively, when $h = 0.8$ mm. This indicates that the flow resistance and leakage control advantages of the fishway-inspired labyrinth seal with a staggered-tooth structure become more pronounced at a relatively large seal clearance compared to that of the single-sided labyrinth seal.



(**a**) Leakage rate (**b**) Leakage rate increment

Figure 14. Variation in leakage rate and its increments for three labyrinth seals with seal clearance.

4.3. Flow Field Analysis of Fishway-Inspired Labyrinth Seals

For labyrinth seals, the flow resistance effects influencing their leakage characteristics primarily include thermodynamic effects, surface friction effects, permeation direct leakage effects, and flow jet contraction effects. In the case of staggered labyrinth seals, the sealing gap does not allow fluid to leak unobstructed and directly, thus the analysis focuses on the other three flow resistance effects. Surface friction effects refer to the flow resistance induced by the viscous friction between the fluid and the solid wall, the intensity of which is proportional to the flow path length. The tooth-tip jet contraction effect refers to the phenomenon where fluid within the tooth chamber experiences local jet contraction and reduced cross-section due to inertia when entering the tooth-top gap. Abrupt expansion, contraction, and bending of the flow path can result in significant local flow losses. Additionally, the narrow main flow channel formed after jet contraction increases resistance along the flow path. The stronger the thermodynamic effects, surface friction effects, and jet contraction effects are and the weaker the permeation direct leakage effect is, the stronger the flow resistance and the smaller the leakage rate.

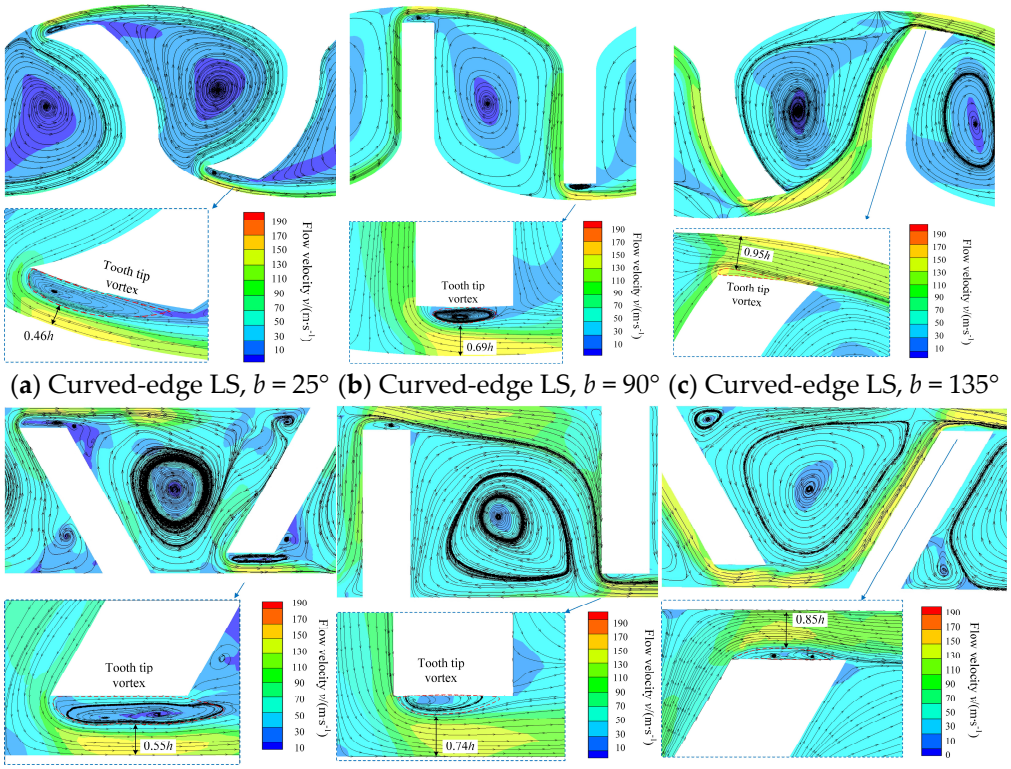
Three labyrinth seals, including those with acutely inclined teeth with the minimum leakage rate, obtusely inclined teeth with the maximum leakage rate, and a straight tooth when $\beta = 90°$, were selected for further study. A comparative analysis was conducted on the flow field distribution across the meridional plane of the third tooth chamber, as well as the mid-plane velocity distribution in both the CELS and SELS under different tooth incline angles, as shown in Figures 15 and 16, respectively, to explore the reasons for differences in flow resistance and leakage control.

As shown in Figure 15, the leak mainstream of the CELS flows along the windward chamber wall, with its flow path length and mainstream velocity increasing monotonically with the incline angle. Thus, the along-path flow resistance of the acute-angle tooth labyrinth seal is significantly greater than that of the obtuse-angle tooth labyrinth seal, resulting in strong surface friction effects. Conversely, the leak mainstream path length in SELS tooth chambers is not sensitive to changes in the tooth incline angle, although the average mainstream velocity does increase, potentially elevating the leakage rate.

When $\beta \leq 90°$, significant flow jet contraction and tooth-top vortex regions were observed at the sealing gap on the tooth top, narrowing the actual flow channel of the mainstream. The vortex regions at the tooth top for $\beta = 25°$ and $90°$ are most evident and expansive in the CELS, leading to the narrowest main flow channel widths of 0.46 h and 0.69 h, respectively. However, the size and intensity of the vortex regions in both the CELS and SELS rapidly diminish with an increasing tooth incline angle, with no evident vortex region at $\beta = 135°$ and the widest main flow channel width of 0.95 h. Consequently, as

depicted in Figure 17, the average gas flow velocity along the flow direction gradually increases, with the CELS at β = 25° displaying significantly lower tooth-top velocity, whereas the SELS at β = 90° exhibits the highest tooth-top velocity.

The dissipation rate of turbulent kinetic energy represents the rate at which turbulent kinetic energy is converted into molecular thermal energy due to molecular viscosity, reflecting the intensity of this conversion into thermal internal energy [8]. Effective viscosity is a comprehensive indicator of laminar and turbulent viscosities, with its value reflecting the degree to which fluid flow becomes turbulent or vortex-dominated. A higher dissipation rate of turbulent kinetic energy or larger effective viscosities contributes to stronger thermodynamic effects of the seal and thus stronger flow resistance.



(**a**) Curved-edge LS, b = 25° (**b**) Curved-edge LS, b = 90° (**c**) Curved-edge LS, b = 135°

(**d**) Straight-edge LS, b = 60° (**e**) Straight-edge LS, b = 90° (**f**) Straight-edge LS, b = 120°

Figure 15. Velocity field distribution of the fishway-inspired seal under different incline angles.

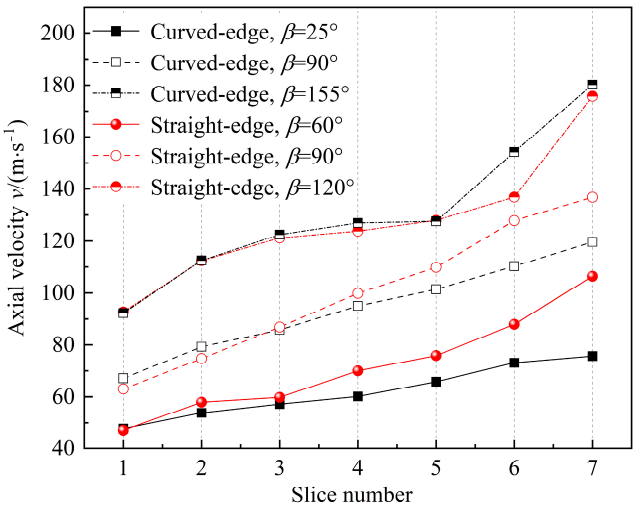


Figure 16. Flow velocity distribution at the mid-plane on the sealing tip gap of the FSLSs.

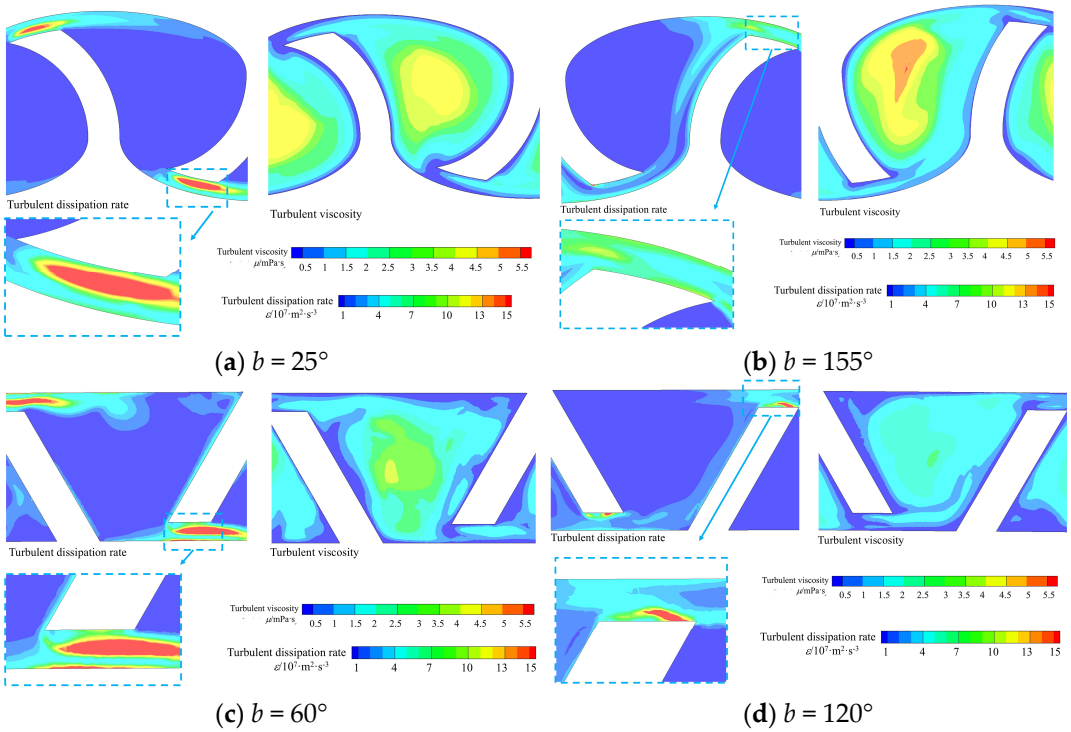
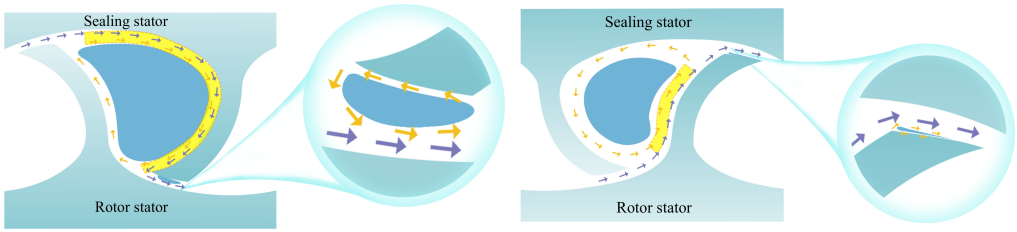


Figure 17. Distribution of turbulent dissipation rate and effective viscosity of the staggered seal under different incline angles.

Figure 17 shows the distribution of the turbulent kinetic energy dissipation rate and effective viscosity within the meridional plane of the third tooth cavity of the labyrinth seal corresponding to the minimum and maximum leakage rates for the CELS and SELS. It reveals that, due to the more fully developed vortices in the tooth cavity of the CELS, the effective viscosity within the cavity is significantly greater than that of the SELS, indicating greater fluid flow resistance. This is one of the reasons why both the maximum and minimum leakage rates of the CELS are smaller than those of the straight-edge version. However, since the vortex velocity within the tooth cavity is relatively low, the dissipation rate of the turbulent kinetic energy is not high. By analyzing the distribution of the turbulent kinetic energy dissipation rate within the tooth gap, it can be seen that the dissipation rate is substantial in the vortex region at the tooth top resulting from flow contraction, indicating a thorough conversion of turbulent kinetic energy into thermal energy. The dissipation rate is notably larger for FSLSs with acute incline angles compared to those with obtuse angles. However, there is no significant difference in the dissipation rate at the tooth top between the CELS with $\beta = 25°$ and the SELS with $\beta = 60°$.

In summary, the differences in leakage characteristics among FSLSs with different incline angles and structures result from the combined effects of multiple flow resistance phenomena. Figure 18 provides a detailed illustration of the comprehensive flow resistance effects for FSLSs with acute and obtuse incline angles. The markedly lower leakage rate for acute-angle incline tooth seals compared to obtuse-angle incline tooth seals can be primarily attributed to the following mechanisms: firstly, the larger vortex area at the tooth top, larger turbulent kinetic energy dissipation rate, narrower main flow channels in the tooth gap, and stronger contraction and thermodynamic effects in the acute-angle incline tooth seals; secondly, the longer main flow path in the tooth cavities of acute-angle incline tooth seals results in stronger surface friction effects.



(**a**) $b < 90°$ (**b**) $b > 90°$

Figure 18. Schematic diagram of the fluid flow model in the sealing gap of the CELS under different incline angles.

4.4. Influence of Geometrical Parameters

Besides the tooth incline angle, the leakage characteristics of the CELS are influenced by other structural parameters. Based on a constant total axial length of the seal, as well as an unchanged aspect ratio of the labyrinth tooth chamber and tooth inclination angle, the impact of the number of labyrinth tooth chambers on the leakage rate was investigated, as shown in Table 4. As the number of labyrinth tooth chambers increases, the leakage rate approximately follows a monotonically decreasing trend. This is because the pressure drop in the fishway-inspired labyrinth seal is primarily attributed to the jet contraction effect at each tooth tip, and an increase in the number of teeth significantly enhances this flow resistance effect. However, having too many teeth can lead to a reduction in tooth thickness and thus a decrease in strength, while also increasing the likelihood of rubbing between rotor and stator teeth.

Table 4. Variation in seal leakage rate under different conditions of axial tooth count.

Tooth Count	Mass Leakage Rate q_m/(g·s^{-1})
6	0.80811
8	0.69007
10	0.58035
12	0.49001
14	0.41985

Figure 19 illustrates how the leakage rate of the CELS varies with changes in the inlet coefficient, aspect ratio, tooth thickness, and seal clearance. This indicates that the leakage rate increases approximately linearly as the aspect ratio and tooth thickness increase and shows a decelerating increase with the increases in seal clearance while remaining insensitive to the changes in the inlet coefficient. Among the given parameters, the seal clearance has the most significant impact on the leakage rate, followed by the inlet coefficient, and the tooth thickness has the least impact. Hence, to achieve a lower leakage rate, relatively low values of the aspect ratio ($w < 0.6$), tooth thickness ($t < 1.5$ mm), and seal clearance ($h < 0.5$ mm) and relatively high values of the tooth count ($n > 10$) should be selected. Conversely, a smaller inlet coefficient ($\delta < 1.0$) is recommended to enhance the strength of labyrinth teeth.

By comparing the velocity field distribution in the meridional plane of the third tooth cavity of CELSs under different structural parameters, this study aims to explore the mechanism affecting the leakage characteristics. Figure 20 shows the velocity field of CELSs under different inlet coefficients. As the inlet coefficient increases, the area of the labyrinth tooth cavity is enlarged, slightly extending the mainstream path within the cavity and enhancing the surface friction effect. However, when the inlet coefficient exceeds 1, noticeable flow separation occurs at the tooth root, and the surface friction effect no longer increases. It is noteworthy that changes in the inlet coefficient do not significantly impact

the structural shape and the flow field distribution at the tooth top. This further indicates that the differences in the flow field at the tooth gap are a primary reason for the variations in leakage characteristics among different seal structures.

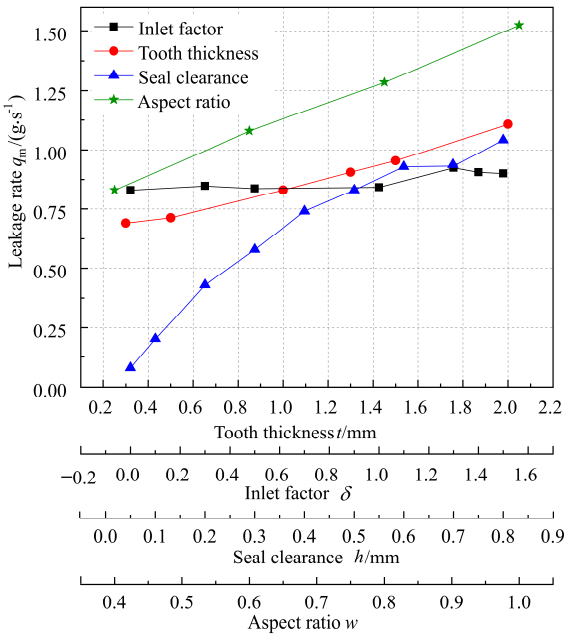


Figure 19. Effect of key geometrical parameters on leakage rate of CELS.

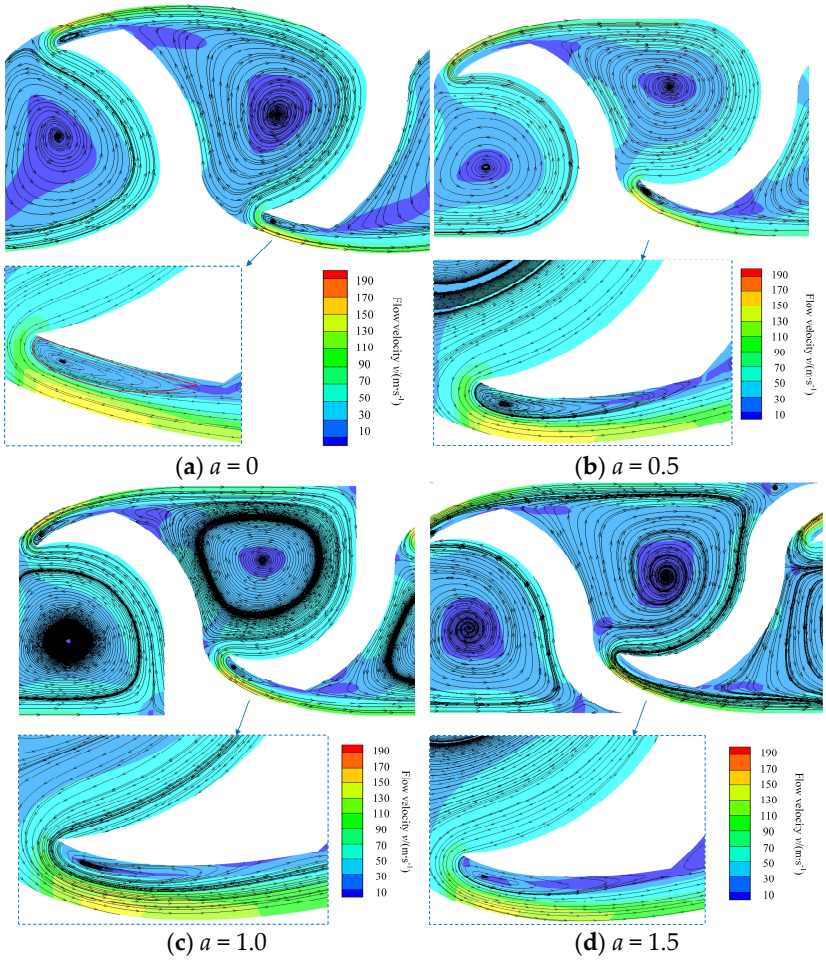


Figure 20. Velocity field distribution on the sealing gap of CELS under different shape factors.

Figure 21 presents the velocity field of CELSs under different aspect ratios. As the aspect ratio increases, the labyrinth tooth cavity gradually transforms from an elliptical to a circular shape. On the one hand, it modifies the vortex flow within the tooth cavity and extends the mainstream flow path along the cavity wall, enhancing the surface friction effect, which may reduce the leakage rate. More importantly, it lessens the curvature at the entrance of the tooth gap, thereby rapidly reducing both the area and intensity of the vortex at the tooth top and increasing the area of the mainstream channel at the tooth top. For instance, when w = 0.4, the vortex width at the tooth top occupies more than half of the tooth gap, while when w = 1.0, no significant vortex is visible at the tooth top. The diminishment both in the flow contraction effect and thermodynamic effect leads to an increased leakage rate, which is also the primary reason for the sensitivity of leakage rate changes to aspect ratio variations.

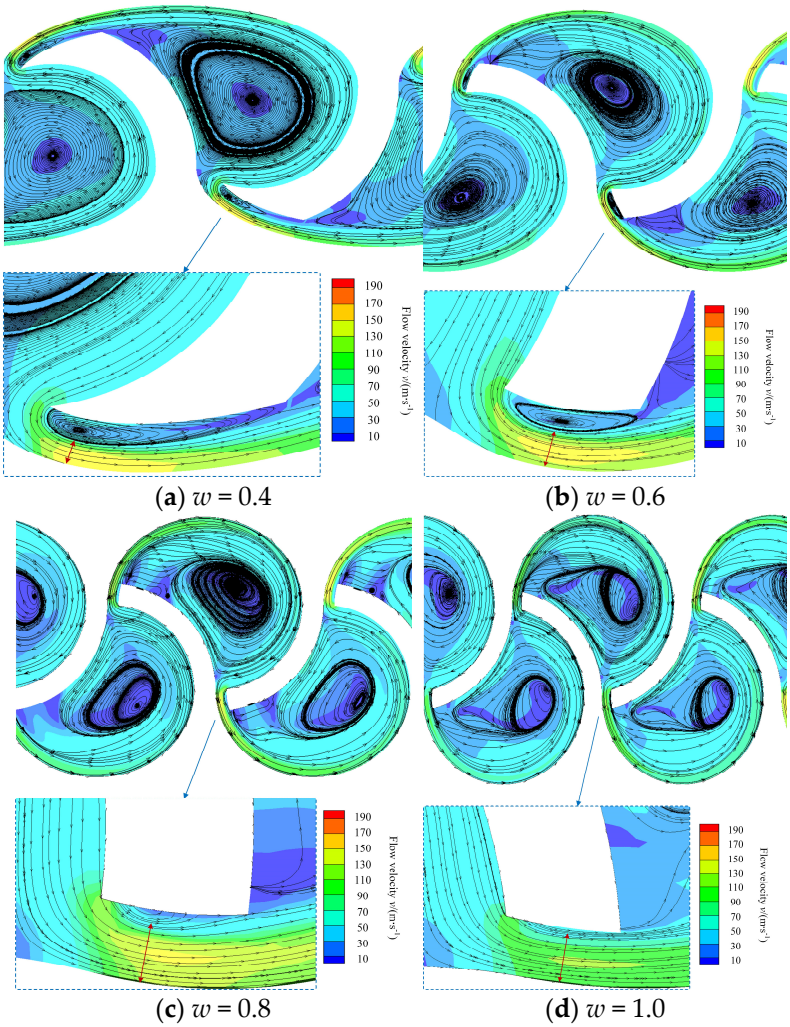


Figure 21. Velocity field distribution on the sealing gap of CELS under different aspect ratios.

Figure 22 illustrates the flow field distribution of CELSs under different tooth thickness conditions. As the tooth thickness increases, prominent flow contraction phenomena and vortex dissipation zones are evident at the tooth tops of the seals. However, the development of vortices along the seal clearance direction slightly weakens, reducing the flow contraction effect. On the other hand, the reduction in flow curvature at the entrance of the tooth gap decreases local flow resistance. The combined impact of these changes slightly increases the seal leakage rate, although the extent of influence is not significant.

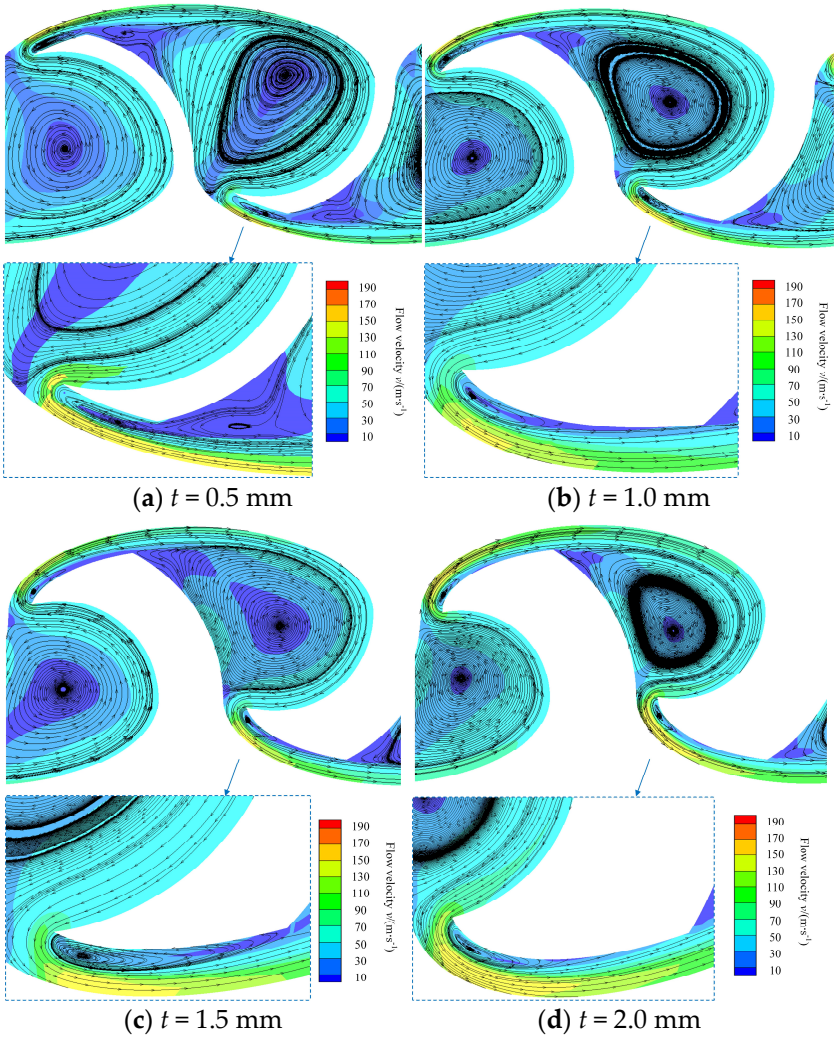


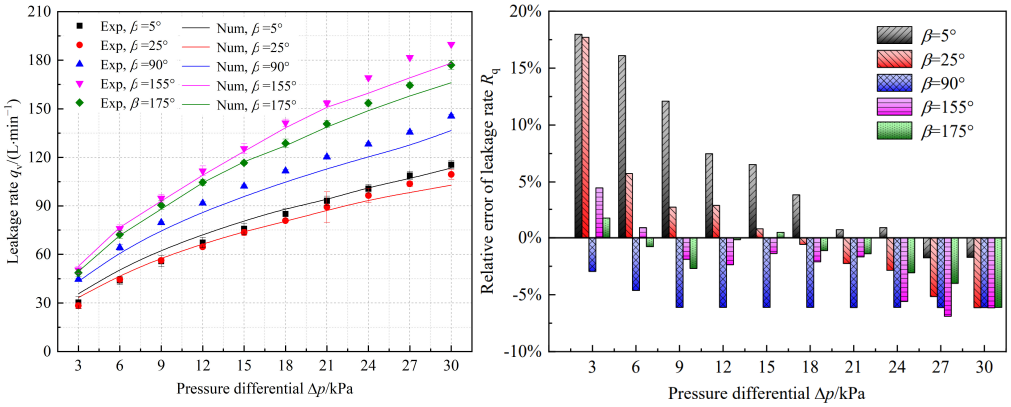
Figure 22. Velocity field distribution on the sealing gap of CELS under different tooth thicknesses.

4.5. Experimental Results of Leakage Rate

Experiments were conducted using flat-plate specimens of the CELSs with different incline angles. The inlet pressure was maintained at 300 kPa, while the outlet pressure was gradually reduced from 297 kPa to 270 kPa, and the volumetric leakage rates under varying seal pressure differentials were obtained. To validate the accuracy of the numerical simulation model of the leakage rate, the measured values, simulated values, and relative errors of the volumetric leakage rate for the CELSs with five incline angles were analyzed as functions of seal pressure differential, as shown in Figure 23. The relative error of leakage rate R_q is defined as the relative error between the simulated and measured leakage rates under identical conditions for the same seal structure.

From Figure 23a, it can be observed that with an increasing pressure differential, both the simulated and measured values of the leakage rate for labyrinth seals under various incline angles exhibit a decelerating increase, with a good degree of consistency, although the simulated values tend to be slightly lower at a large pressure differential. Relative leakage rate errors show positive values at a small pressure differential, with errors reaching up to 17% for certain angles, indicating higher simulated leakage rates. As the seal pressure differential increases, the relative errors transition from positive values to negative values, stabilizing around −6%. This phenomenon is attributed to the fact that at lower pressure differentials, the turbulence in the flow through the sealing gap is not fully developed, leading to larger deviations in the simulated leakage rate based

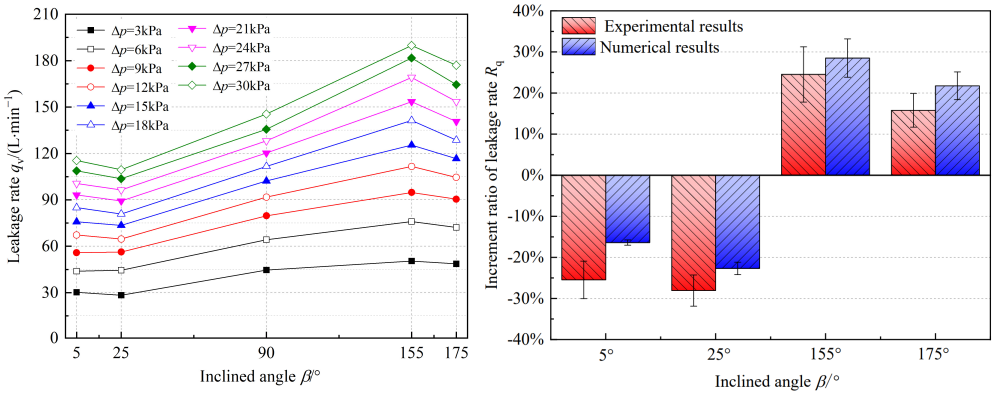
on the turbulence model. As the pressure differential increases and flow becomes more turbulent, simulated and measured results converge and stabilize. The comparison suggests that the adopted turbulence model demonstrates high prediction accuracy at large seal pressure differentials.



(**a**) Leakage rate (**b**) Relative error of leakage rate

Figure 23. Variation in the measured and simulated leakage rates of CELS with increasing pressure differentials under different incline angles.

To verify the reliability of the simulated variation in leakage rate with incline angles, Figure 24 presents the test values of the leakage rate and its relative increments with incline angles under different seal pressure differentials. The relative increment in the leakage rate is defined as the relative increase in the leakage rate for a given incline angle compared to that at $\beta = 90°$ under the same conditions. The average value and standard deviation of relative increments were obtained from data across 10 different pressure differentials. It shows that under all tested pressure differentials, the leakage rate exhibits a trend of initially decreasing, then increasing, and finally decreasing again with an increasing incline angle, reaching minimum and maximum values at $\beta = 25°$ and 155°, respectively, thereby confirming the reliability of the simulated trend. Further analysis reveals that for $\beta = 5°$ and 25°, the experimental decrease in leakage rate is about 5% to 10% larger than the simulated values, with a maximum reduction of 29%. In contrast, for $\beta = 155°$ and 175°, the experimental increase in the leakage rate is approximately 5% lower than the simulated values. Overall, compared to the traditional staggered labyrinth seals when $\beta = 90°$, FSLS with $\beta = 25°$ achieves a maximum reduction in the leakage rate of up to 30%.



(**a**) Leakage rate (**b**) Increment ratio of leakage rate

Figure 24. Variation in the measured and simulated leakage rate of CELS with incline angle under different pressure differentials.

5. Conclusions

(1) Inspired by the ecological fishway with high flow-resistance capacity in nature, a fishway-inspired staggered labyrinth seal structure was proposed. Numerical simulations and experimental tests indicated that the CELS and SELS achieve the minimum leakage rate at $\beta = 25^\circ$ and $\beta = 60^\circ$, respectively. Compared to the typical staggered straight-tooth labyrinth seal at $\beta = 90^\circ$, the CELS reduces the leakage rate by 25% to 30%, while the SELS achieves a reduction of 10% to 25%.

(2) The leakage rate of single-sided straight-through labyrinth seals increases at an accelerating rate with increasing seal clearance. In contrast, the leakage rate of double-sided FSLSs increases at a decelerating rate, making them a sealing structure with more pronounced flow resistance and leakage control capacity at a relatively large seal clearance.

(3) The primary reasons for the superior flow resistance and leakage control characteristics of the FSLS include the bent flow paths and flow contraction (tip clearance contraction effect) as the fluid flows from the labyrinth tooth cavity to the tooth top gap, and the high turbulent kinetic energy dissipation rate in the vortex regions at the tooth top (thermodynamic effect). Changes in surface friction effects along cavity walls and the intensity of vortex dissipation due to the altered shape of the tooth cavity are minor factors.

(4) The leakage characteristics of the FSLS are also affected by the seal clearance, tooth thickness, and aspect ratio. The seal clearance has the most significant impact, followed by the aspect ratio, and the effect of the inlet coefficient is negligible. Optimal leakage characteristics can be achieved with seal clearance $h < 0.5$ mm, tooth thickness $t < 1.5$ mm, and aspect ratio $w < 0.6$.

Author Contributions: Methodology, J.J., X.Z., M.Z. and C.L.; Software, Z.Y.; Investigation, X.Z.; Resources, X.Z.; Writing—original draft, Z.Y.; Writing—review & editing, J.J. and X.Z.; Project administration, J.J.; Funding acquisition, J.J. All authors have read and agreed to the published version of the manuscript.

Funding: This research was funded by National Natural Science Foundation of China grant number U2241246, 52075491, and the Natural Science Foundation of Zhejiang Province grant number LMS25E050013. The APC was funded by National Natural Science Foundation of China grant number U2241246, 52075491, and the Natural Science Foundation of Zhejiang Province grant number LMS25E050013.

Data Availability Statement: The original contributions presented in this study are included in the article. Further inquiries can be directed to the corresponding author.

Acknowledgments: This work is supported by the National Natural Science Foundation of China (U2241246, 52075491) and the Natural Science Foundation of Zhejiang Province (LMS25E050013).

Conflicts of Interest: The authors declare no conflict of interest.

References

1. Li, G.Q.; Zhang, Q.; Lei, Z.J.; Huang, E.L.; Wu, H.W.; Xu, G. Leakage Performance of Labyrinth Seal for Oil Sealing of Aero-Engine. Propuls. *Propuls. Power Res.* **2019**, *8*, 13–22. [CrossRef]
2. Sun, D.; Zhou, M.; Zhao, M.; Zhao, H.; Lu, J.; Fei, C.W.; Li, H. Numerical and Experimental Investigations on Windage Heating Effect of Labyrinth Seals. *J. Aerospace Eng.* **2020**, *33*, 04020057. [CrossRef]
3. Kim, H.J.; Kang, Y.J.; Kim, W.; Lim, W.S.; Park, S.; Kwak, J.S. Improvement of Labyrinth Seal Performance Using the Partial Honeycomb Lands. *Aerosp. Sci. Technol.* **2024**, *148*, 109082. [CrossRef]
4. Nayak, K.C. Effect of Rotation on Leakage and Windage Heating in Labyrinth Seals with Honeycomb Lands. *J. Eng. Gas Turbines. Power.* **2020**, *142*, 081001. [CrossRef]
5. Kim, S.; Kim, K.; Son, C. Three-Dimensional Unsteady Simulation of a Multistage Axial Compressor with Labyrinth Seals and Its Effects on Overall Performance and Flow Characteristics. *Aerosp. Sci. Technol.* **2019**, *86*, 683–693. [CrossRef]

6. Huo, C.J.; Sun, J.J.; Song, P.; Sun, W.Y. Influence of Tooth Geometrical Shape on the Leakage and Rotordynamic Characteristics of Labyrinth Seals in a Cryogenic Liquid Turbine Expander. *Int. J. Refrig.* **2023**, *145*, 105–117. [CrossRef]
7. Zhang, B.; Dou, Y.Y.; Hong, Q.; Ji, H.H. Experimental Investigation of Effect of Tooth Geometrical Parameters to Flow Characteristics in Slant Labyrinth Seals. *Concurr. Comput. Pract. Exp.* **2018**, *30*, e4951. [CrossRef]
8. Chougule, H.H.; Mirzamoghadam, A.V. CFD Leakage Predictions of Labyrinth Seals Having Straight and Inclined Notched Teeth with Staggered Honeycomb Land. In Proceedings of the ASME Turbo Expo: Turbomachinery Technical Conference and Exposition, Oslo, Norway, 11–15 June 2018.
9. Zhang, X.; Jiang, J.B.; Peng, X.D.; Zhao, W.J.; Li, J.Y. Leakage Reduction by Optimization of Hole-Pattern Damping Seal with Inclined Hole Cavity. *Int. J. Heat Mass Transf.* **2021**, *169*, 120924. [CrossRef]
10. Zhao, Y.; Wang, C. Shape Optimization of Labyrinth Seals to Improve Sealing Performance. *Aerospace* **2021**, *8*, 92. [CrossRef]
11. Kim, H.J.; Kang, Y.J.; Kim, W.; Jo, Y.R.; Park, S.; Kwak, J.S. Mass Flow Function Correlation for Solid and Honeycomb Land Labyrinth Seals Including Fin Front Angle, Clearance, Fin Number and Honeycomb Geometry. *Machines* **2023**, *11*, 880. [CrossRef]
12. Zhang, X.; Jiang, J.B.; Peng, X.D.; Ni, Z.J. Experimental and Numerical Simulation Study on the Influence of Structural Factors on the Leakage Characteristics of Clearance Seals. *Flow Meas. Instrum.* **2023**, *94*, 102465.
13. Zhang, X.; Jiao, Y.H.; Du, H.Z.; Huo, G.H.; Xu, Y.Y.; Che, R.W. Transient Investigations of Teeth on Rotor and Teeth on Stator Modified Labyrinth Seals. *Tribol. Int.* **2024**, *192*, 109296. [CrossRef]
14. Liu, H.; Li, G.Q.; Li, H.; Li, A.; Lu, X.E. Investigation on The Discharge and Windage Heating Characteristics of Staggered Labyrinth Seals under Adiabatic and Heat Transfer Models. *Int. J. Heat Fluid Flow* **2024**, *109*, 109514. [CrossRef]
15. Liu, H.; Li, G.Q.; Li, H.; Li, A.; Lu, X.E. Conjugate Heat Transfer Analysis on the Action Mechanism of Centrifugal Force and Centrifugal Buoyancy in Staggered Labyrinth Seals. *Case Stud. Therm. Eng.* **2024**, *61*, 105001. [CrossRef]
16. Gu, Q.L.; Yang, J.A.; Zhang, W.F.; Zhang, M.J.; Yin, H. A Fluidic Oscillator Seal Concept for Sealing Performance Enhancement by Controlling the Kinetic Energy Carry-Over Effect. *Tribol. Int.* **2024**, *191*, 109205. [CrossRef]
17. Wu, T.C.; San Andrés, L. Gas labyrinth seals: On the Effect of Clearance and Operating Conditions on Wall Friction Factors-A CFD Investigation. *Tribol. Int.* **2019**, *131*, 363–376. [CrossRef]
18. Jia, X.Y.; Zheng, Q.; Jiang, Y.T.; Zhang, H. Leakage and Rotordynamic Performance of T Type Labyrinth Seal. *Aerosp. Sci. Technol.* **2019**, *88*, 22–31. [CrossRef]
19. Yan, S.B.; Ye, Z.F.; Wang, D.Z.; Su, H.H.; Zhou, W.J. Numerical Investigations of Static and Dynamic Characteristics of a Novel Staggered Labyrinth Seal with Semi-Elliptical Structure. *Lubricants* **2024**, *12*, 169. [CrossRef]
20. Su, H.H.; Shi, J.L.; Zhou, W.J. Study on Leakage Performance and Rotordynamic Characteristics of a Novel Semi-Y Type Labyrinth Seal. *Lubricants* **2022**, *10*, 234. [CrossRef]
21. Zhang, M.J.; Yang, J.A.; Zhang, W.F.; Gu, Q.L. Turbomachines Seal Flow Resistance Enhancement and Leakage Reduction Based on Flow Control Method with Bow-Shaped Auxiliary Teeth. *Energy* **2024**, *300*, 131631. [CrossRef]
22. Moscatelli, E.; Andreasen, C.S.; Aage, N.; Picelli, R.; Silva, E.C.N. Topology Optimization of Labyrinth Seals Using Interface Identification Techniques. *Comput. Methods Appl. Mech. Eng.* **2024**, *420*, 116716. [CrossRef]
23. Cao, X.J.; Li, J.L.; Liu, J.L. Bio-Inspired Optimization Design and Fluid-Solid-Thermal Multi-Field Verification Analysis of Labyrinth Seal. *Mater. Des.* **2022**, *220*, 110907. [CrossRef]
24. Jiang, J.B.; Peng, X.D.; Li, J.Y.; Chen, Y. A Comparative Study on The Performance of Typical Types of Bionic Groove Dry Gas Seal Based on Bird Wing. *J. Bionic. Eng.* **2016**, *13*, 324–334. [CrossRef]
25. Jiang, J.B.; Peng, X.D.; Li, J.Y.; Chen, Y. Leakage and Stiffness Characteristics of Bionic Cluster Spiral Groove Dry Gas Seal. *Chin. J. Mech. Eng.* **2018**, *31*, 21. [CrossRef]
26. Zhao, H.Q.; Xu, Y.; Lu, Y.; Lu, S.S.; Dai, J.; Meng, D.H. Numerical Study of Vertical Slot Fishway Flow with Supplementary Cylinders. *Water* **2022**, *14*, 1772. [CrossRef]
27. Nikola, T. Valvular Conduit. US Patent 19160079703, 3 February 1920.
28. Truong, T.Q.; Nguyen, N.T. Simulation and Optimization of Tesla Valves. In Proceedings of the Nanotechnology Conference and Trade Show (Nanotech 2003), San Francisco, CA, USA, 23–28 February 2003.
29. Monika, K.; Chakraborty, C.; Roy, S.; Sujith, R.; Datta, S.P. A Numerical Analysis on Multi-Stage Tesla Valve Based Cold Plate for Cooling of Pouch Type Li-Ion Batteries. *Int. J. Heat Mass Transf.* **2021**, *177*, 121560. [CrossRef]
30. Vries, S.D.; Florea, D.; Homburg, F.; Frijns, A. Design and Operation of a Tesla-Type Valve for Pulsating Heat Pipes. *Int. J. Heat Mass Transf.* **2017**, *105*, 1–11. [CrossRef]
31. Thompson, S.M.; Ma, H.B.; Wilson, C. Investigation of a Flat-Plate Oscillating Heat Pipe with Tesla-Type Check Valves. *Exp. Therm. Fluid Sci.* **2011**, *35*, 1265–1273. [CrossRef]

32. Wang, Y.; Xie, X.F.; He, Y.M.; Huang, Z.X.; Xu, H.; Chai, D.Z.; Yang, H.S. A New Non-Contact Fluid Seal Technology Based on Tesla Valve. *Tribology* **2023**, *43*, 975–985.
33. Wang, Y.; He, Y.M.; Xie, X.F.; Huang, Z.X.; Xu, H.; Hu, Q.; Ma, C.B. Design and Simulation of a New Near Zero-Wear Non-Contact Self-Impact Seal Based on The Tesla Valve Structure. *Lubricants* **2023**, *11*, 102. [CrossRef]

Disclaimer/Publisher's Note: The statements, opinions and data contained in all publications are solely those of the individual author(s) and contributor(s) and not of MDPI and/or the editor(s). MDPI and/or the editor(s) disclaim responsibility for any injury to people or property resulting from any ideas, methods, instructions or products referred to in the content.